Check for updates

Small

NANO · MICRO small
www.small-journal.com

RESEARCH ARTICLE

Stepwise Activation-Guided Zn Deposition for Ultra-High Capacity in Flowless Zn–Br Batteries

Jaewoong Han[1,5] | Mingyu Lee[1,2] | Hyuntae Lee[3] | Youyeong Shin[2] | Suhwan Kim[4] | Kyungjae Shin[5] | Chanyeon Kim[1] | Hee-Tak Kim[5] | Yong Min Lee[2,4] | Hongkyung Lee[1,2,3]

[1]Department of Energy Science & Engineering, Daegu Gyeongbuk Institute of Science and Technology (DGIST), Daegu, Republic of Korea | [2]Department of Battery Engineering, Yonsei University, Seoul, Republic of Korea | [3]Department of Materials Science and Engineering, Yonsei University, Seoul, Republic of Korea | [4]Department of Chemical and Biomolecular Engineering, Yonsei University, Seoul, Republic of Korea | [5]Department of Chemical and Biomolecular Engineering, Korea Advanced Institute of Science and Technology (KAIST), Daejeon, Republic of Korea

Correspondence: Chanyeon Kim (chanyeon@dgist.ac.kr) | Hee-Tak Kim (heetak.kim@kaist.ac.kr) | Yong Min Lee (yongmin@yonsei.ac.kr) | Hongkyung Lee (hongkyung.lee@yonsei.ac.kr)

Received: 31 August 2025 | **Revised:** 16 December 2025 | **Accepted:** 12 January 2026

Keywords: 3D Zn host | bottom-to-top Zn deposition | flowless Zn-Br batteries | top-plating | ultrahigh-capacity

ABSTRACT

Flowless Zn–bromine batteries (FL–ZBBs) are attracting attention as a route to overcome the inherent system-level limitations of conventional flow batteries. However, the difficulty of achieving high $ZnBr_2$ utilization and ultra-high areal capacity jeopardize practical feasibility: Under practically relevant conditions, Zn-hosting electrodes suffer from top-plating issues and dendrite-triggered "dead" Zn accumulation, which deteriorates reversible Zn plating/stripping. This work presents a stepwise activation (SWA) electrode that guides top-plating-free, bottom-to-top sequential Zn deposition. The SWA architecture is designed by introducing insulating porous membranes physically separating stacked CF layers while electrically linking through controlled partial Zn penetration. Benefiting from SWA-guided Zn deposition, FL-ZBBs can stably retain higher Coulombic and energy efficiencies even at a high current cycling (20 mA cm^{-2}) over 10 000 cycles. For the first time, we demonstrate a stable ultra-high capacity cycling (100 mAh cm^{-2}) of FL-ZBB with SWA electrode by maximizing the $ZnBr_2$ utilization (~33%). This simple, scalable SWA design offers broad applicability, enabling high-capacity operation in flowless batteries and extending to other metal-deposition-limited redox systems.

1 | Introduction

Sustainable, safe energy storage systems (ESSs) power the transition to the renewable energy era [1–3]. Compared to lithium–ion batteries (LIBs) with organic electrolytes, aqueous batteries have long been considered an ultimate solution for ESSs due to their inherent non–flammability [4]. Redox flow batteries (RFBs) utilizing the zinc (Zn) and bromine (Br) redox couple in aqueous media are particularly attractive due to their environmental benignity and cost–effectiveness [5–8]. Nonetheless, the auxiliary components in RFBs, such as electrolyte tanks and pumping systems, reduce energy density and increase system complexity, thereby hindering widespread adoption. In this context, flowless Zn–Br batteries (FL–ZBBs) are emerging as a promising alternative [9–13]. Indeed, the simplified architecture and use of low–cost materials (e.g., $ZnBr_2$) in FL–ZBBs enable cost–effective (~85$/kWh) and scalable energy storage solutions.

Jaewoong Han, Mingyu Lee, and Hyuntae Lee contributed equally to this work.

© 2026 Wiley-VCH GmbH

In terms of commercial viability, however, most technical challenges faced by FL–ZBBs are shared with those of conventional RFB systems, including poor reliability and cycle lifespan, primarily due to Br crossover, gassing and the low reversibility of the Zn metal anode [14, 15]. The absence of the external pump and electrolyte reservoirs can exacerbate the crossover of Br species, such as Br_2 and polybromides (Br_n^-) [7, 9]. Br crossover can occur during cell standby and even during charging, directly leading to active material loss and substantial capacity fading [16]. Moreover, water–splitting side reactions in aqueous electrolytes cause the evolution of hydrogen and oxygen gases, which get trapped in the absence of flow. This increases cell pressure, causes electrolyte leakage, and can ultimately lead to cell failure [17, 18].

The most striking challenge remains the reversibility of Zn deposition and dissolution. Benefiting from its high specific capacity (820 mAh g^{-1} and 5,885 mAh cm^{-3}) [19–22], achieving high Zn utilization by increasing Zn plating capacity is essential for realizing practical energy density gains [7]. Nonetheless, higher Zn plating capacity is risky owing to uncontrolled Zn dendrite growth, which can puncture the separator (or membrane) and trigger internal short circuits. Moreover, excessive dendritic growth and penetration can accelerate Br crossover and gas evolution, resulting in reduced cycle life, compromised cycling stability, and ultimately premature cell failure. This cascade of detrimental effects becomes more severe at high current densities (>10 mA cm^{-2}), further limiting power density. Therefore, suppressing Zn dendrite growth is a prerequisite for ensuring the reliability and longevity of FL–ZBBs.

Recently, numerous strategies have been proposed and actively explored to suppress Zn dendrite growth [10, 21–26]. Among them, 3D Zn host structures, such as carbon felt or carbon cloth, can offer a high surface area to facilitate Zn deposition, reduce nucleation overpotential, and ensure uniform current distribution [27, 28]. The major drawback, however, is 'top–plating', which leads to preferential Zn deposition at the top of the electrode [7, 29, 30]. This phenomenon arises from uneven electric field distribution and localized current density at the upper surface. This not only limits spatial utilization but also undermines the advantages of the 3D host architecture, while ironically accelerating dendrite growth. To overcome this drawback, strategies such as selective insulation of the top surface [31], decoration with Zn–attracting materials (i.e., zincophilic materials) at the bottom region [32], and introduction of surface carbon defects to provide high Zn–affinity sites [26, 28] have been developed. Nevertheless, these approaches remain limited in achieving both high Zn utilization and high Zn plating capacity.

In this work, we introduce a novel electrode design that enables bottom–to–top stepwise activation (SWA) of Zn deposition, targeting a top–plating–free, ultra–high Zn plating capacity. The SWA electrode is constructed by alternately stacking electron–conducting carbon felt (CF) layers and porous, thin insulating films (Figure 1). Porous insulating layers inserted between CF layers guide Zn plating from the bottom and SWA upon Zn plating via layer–by–layer electron tunneling, enabling full electrode utilization. Zn deposition initiated at the bottom layer is crucial to alleviate Zn dendrite growth and electrochemically inactive 'dead' Zn formation. Thus, the SWA electrode consistently exhibits higher Zn Coulombic efficiency (CE) under various cell conditions. Moreover, FL–ZBBs employing the SWA electrode outperform those using conventional CF electrodes, stably retaining higher cell CE and energy efficiency (EE) even at a high-current cycling (20 mA cm^{-2}) over 10,000 cycles. Notably, FL–ZBB with SWA electrode demonstrated a stable cycling without short–circuiting failure even under challenging conditions, ultra–high Zn plating capacity (100 mAh cm^{-2}). The SWA electrode design enables high–capacity FL–ZBBs and highlights its potential for broader applications in battery systems that require excessive metal deposition.

2 | Results and Discussion

To meet the technical cost requirements of ESSs, FL–ZBBs with optimized cell architectures target an extremely low levelized cost of energy storage (LCOES) of 0.017$/kWh/cycle/%, which is significantly lower than that of vanadium redox flow batteries (0.065), Zn–Br flow batteries (0.052), and LIBs (0.58) [9, 12, 33–35]. FL–ZBBs employ bromine chemistry with bromide anions in various oxidation states (Br^-, Br_2, Br_3^-, Br_5^-, and Br_7^-) at the positive electrode and Zn^{2+}/Zn redox reactions at the negative electrode [7, 14, 17, 18]. The cell architecture, designed to realize this mechanism, is schematically illustrated in Figure S1. To ensure sufficient reaction sites for each half–cell reaction, commercially viable CF electrodes were positioned at both the positive and negative sides. The electrolyte, which consists of 2.8 M $ZnBr_2$ dissolved in deionized (DI) water, serves as the active material source, providing both Zn and Br ions. When the state–of–charge exceeds 30%, the battery delivers a capacity of 100 mAh, which aligns with the expected Zn utilization. Higher capacity and Zn utilization directly lower the cost–per–kWh, contributing to the targeted LCOES.

In FL–ZBBs, the electrolyte itself functions as the active material and must be stored within the electrode chambers, making the use of a thick CF structurally necessary [7]. Achieving higher cell capacity and Zn utilization requires a thick CF electrode (~4.6 mm) capable of accommodating sufficient Zn through abundant reaction sites (Figure 1a). Nonetheless, due to lower resistance near the counter electrode, Zn preferentially deposits on the upper CF region (top–plating) rather than uniformly from the bottom (Figure 1b). Over long–term cycling, this top–plating phenomenon exacerbates dendrite growth and the formation of electrochemically inactive 'dead' Zn, ultimately leading to premature cell failure. In contrast, the SWA electrode design partitions the CF layers with insulating films, delaying the electrical activation of the upper layers while promoting Zn deposition at the bottom CF layer (Figure 1c). As Zn plating progresses, adjacent porous insulating films deliberately allow Zn protrusion, which forms electron tunneling pathways that sequentially activate the upper CF layers. This results in bottom–to–top SWA, enabling greater Zn accommodation and improved electrode utilization without the top–plating issue (Figure 1d). For proof–of–concept, we selected the optimal insulating interlayer by evaluating the physical properties of various commercial membranes, focusing on the trade–off between porosity and mechanical strength (Table S1). While glass fiber separators (GF/F) offer high porosity (>90%), favorable for ion transport, they lack the mechanical strength (~0.18 MPa) required to block dendrites. Conversely, polypropylene separators (PP3501) provide high tensile strength

16136829, 2026, 15, Downloaded from https://onlinelibrary.wiley.com/doi/10.1002/smll.202510641 by Daegu Gyeongbuk Institute Of, Wiley Online Library on [22/07/2026]. See the Terms and Conditions (https://onlinelibrary.wiley.com/terms-and-conditions) on Wiley Online Library for rules of use; OA articles are governed by the applicable Creative Commons License

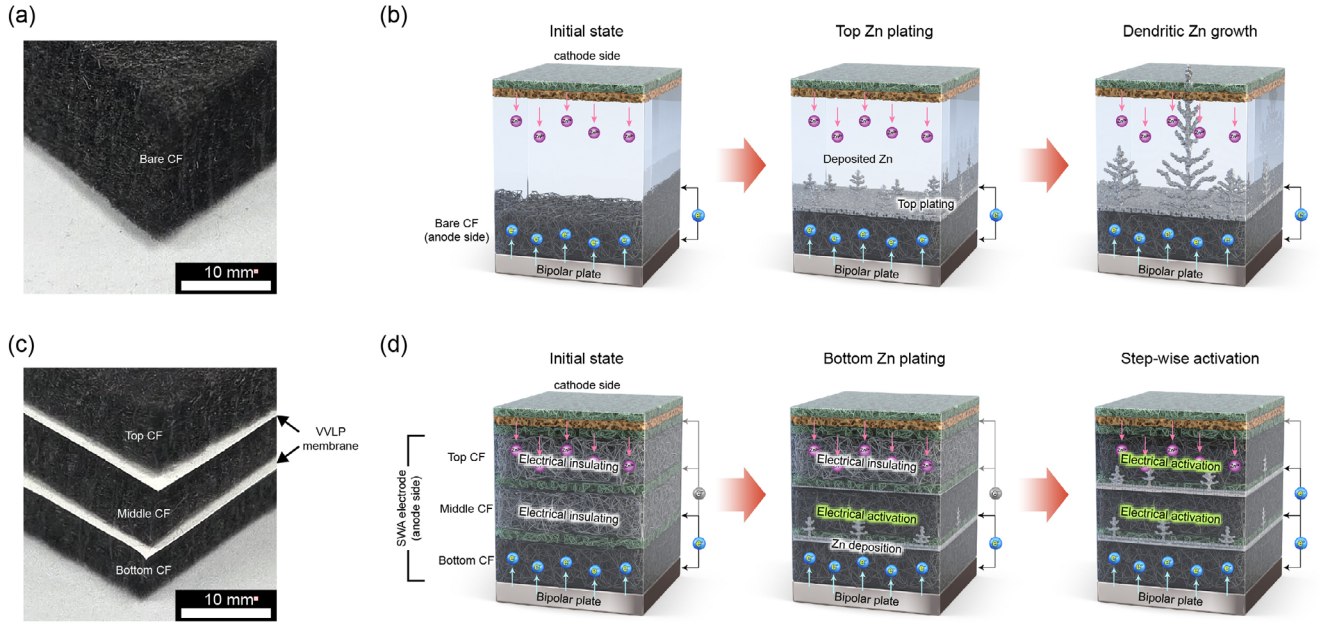

FIGURE 1 | Optical image of (a) Bare CF electrode. (b) Schematic illustration of potential issues arising during long–term cycling of bare CF under high Zn deposition conditions. Optical image of (c) SWA electrode. (d) Design strategies for Zn dendrite suppression and high–capacity deposition using the SWA electrode under long–term cycling.

(103 MPa) but suffer from low porosity (55%) and significant mechanical anisotropy, where the transverse strength is nearly an order of magnitude lower than the machine direction strength [36]. In contrast, the hydrophilic polyvinylidene fluoride (PVDF, VVLP) membrane effectively balances these properties, featuring a high porosity of 70% to prevent concentration polarization and an isotropic tensile strength (~11 MPa) sufficient to withstand multidirectional dendritic stress. Furthermore, its uniform sponge–like pore architecture (~0.1 μm) facilitates homogeneous ion flux compared to the irregular fibrous networks of GF/F or cellulose-based counterparts (NKK). Consequently, the VVLP membrane significantly outperformed the alternatives (Figure S2) and was employed as the interlayer to enable controlled stepwise Zn deposition.

An optical half–cell was constructed for proof–of–concept to visualize Zn plating/stripping in real time at the microscale (Figure 2a). The cell was constructed using a Zn counter electrode and three pieces of carbon paper (CP), replacing excessively thick CF owing to limited space. To mimic the SWA design, three CP pieces were parallelly arranged with spatial separation, instead of using a VVLP layer, and the external lead was connected exclusively to the bottom CP (see Figure S3 for details). When applying a current (10 mA cm^{-2}), Zn plating initially occurs only on the bottom CP, as the middle and top CPs remain electrically isolated. After 5 min, the middle CP becomes activated via contact with plated Zn at the bottom CP, and subsequent Zn plating predominantly occurs on the upper region of the middle CP rather than on the bottom CP. To elucidate these behaviors, we conducted a simulation study using COMSOL Multiphysics (Figure S4). The model domain was constructed by stacking VVLP layers among the three CP layers, incorporating a columnar structure representing Zn dendrites between the bottom and middle CPs. The simulated behavior was consistent with experimental observations, showing the preferential electrodeposition on the middle CP rather than on the bottom CP (Figure S4a). Thickness variations simulated at each interface between layers further supported this trend. While the bottom and top CPs exhibited nearly negligible changes, the middle CP showed a significant positive thickness increase as indicated in red, whereas the counter Zn electrode exhibited a negative value marked in blue related to Zn stripping (Figure S4b). This behavior is attributed to the higher local Zn^{2+} concentration and shorter diffusion length in the upper region of the middle CP (or top CP) compared to the bottom CP. These results demonstrate that under high current density conditions, the relatively lower mass transport rate than reaction rate can activate SWA behaviors in the stacked CP electrode configuration as well as Zn dendrite growth. These findings theoretically verify the operating mechanism of the SWA electrode, demonstrating that electrochemical reactions predominantly occur in the upper region under conditions where electrical connectivity is ensured. During Zn stripping, the reverse sequence was observed, starting from the top CP layer. After Zn stripping from the top CP was completed, the process sequentially progressed to the middle and then the bottom CP, validating the intended functionality of the SWA electrode.

Leveraging the insights into Zn plating and stripping at the SWA electrode, Zn||CF half-cells were constructed on the FL-ZBB platform (Figure S1). Figure 2b presents a direct comparison of the electrochemical responses between SWA and bare CF electrodes. At a current density of 10 mA cm^{-2}, Zn plating and stripping were performed on both electrodes with a capacity of 100 mAh cm^{-2}. While similar Zn CEs (~85%) were observed, the voltage profiles were clearly distinct. The cell with bare CF displayed a single voltage plateau during both plating and stripping, whereas the SWA cell exhibited multiple plateaus, likely due to the sequential activation of the middle and top CF layers. The dQ/dV analysis (inset of Figure 2b) further revealed three distinct peaks for the SWA cell, compared to a single peak for

16136829, 2026, 15, Downloaded from https://onlinelibrary.wiley.com/doi/10.1002/smll.202510641 by Daegu Gyeongbuk Institute Of, Wiley Online Library on [22/07/2026]. See the Terms and Conditions (https://onlinelibrary.wiley.com/terms-and-conditions) on Wiley Online Library for rules of use; OA articles are governed by the applicable Creative Commons License

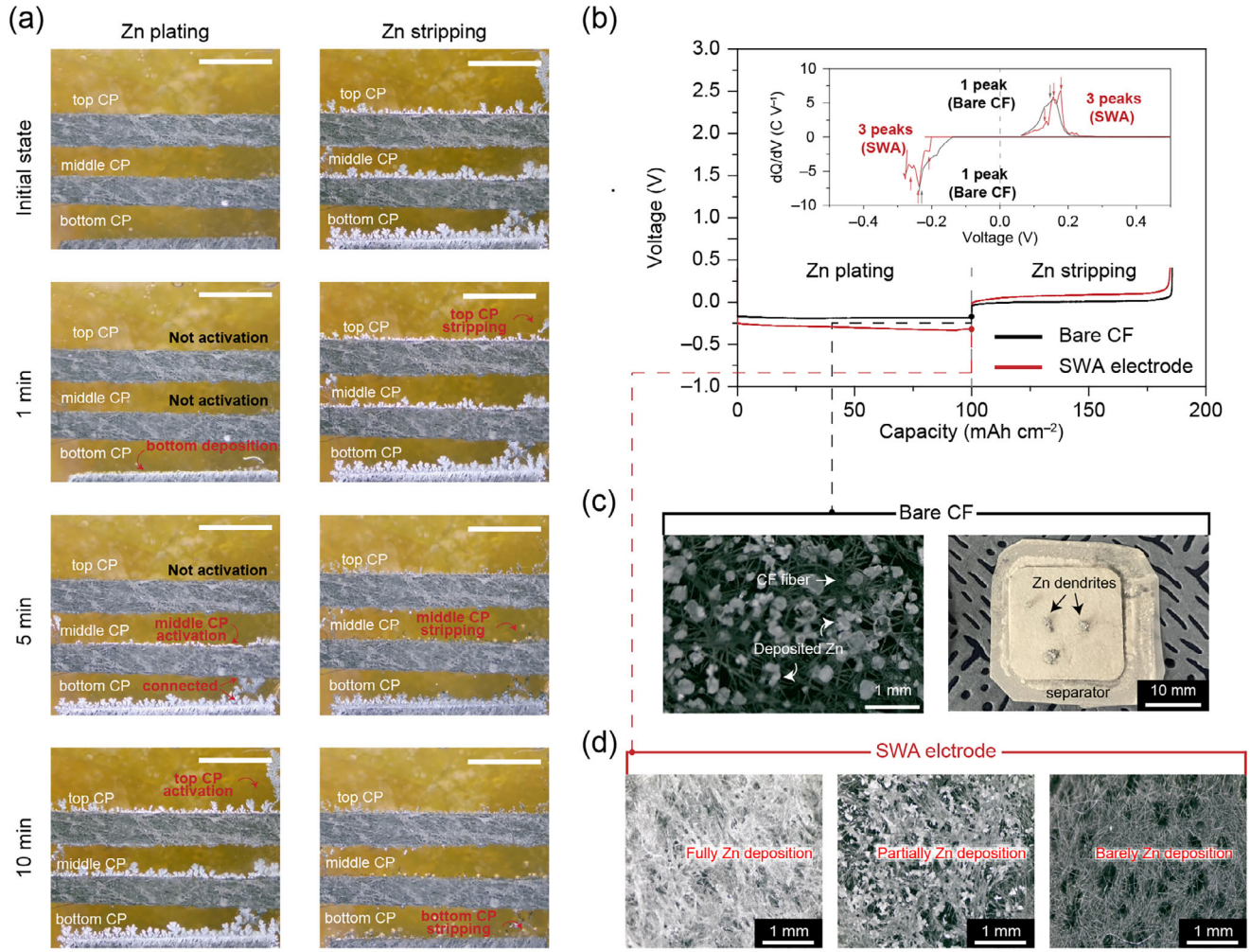

FIGURE 2 | (a) Verification of SWA electrode during the Zn plating/stripping process using an in situ optical microscopy cell. (scale bar size: 200 μm) (b) Voltage profiles and assessment of Zn reversibility and dQ/dV curve analysis at 10 mA cm^{-2}, 100 mAh cm^{-2} condition. (c) Optical microscopy image of bare CF and optical image of penetrated separator and (d) optical microscopy image of each layer of SWA electrode at 10 mA cm^{-2}, 100 mAh cm^{-2} condition.

the bare CF cell, indicating that the electrochemical environment for Zn reactions evolved during the sequential activation process. Whereas the bare CF harvested after Zn plating exhibited top-plating and Zn dendrite penetration (Figure 2c), bottom-to-top Zn deposition in the SWA electrode was confirmed by analyzing the Zn distribution across each CF layer (Figure 2d). Indeed, the individual CF layers were reassembled into separate Zn||CF half-cells for Zn stripping tests to assess layer-specific reversibility (Figure S5). The Zn plating distribution across the bottom, middle, and top CF layers was 68.2%, 16.8%, and 0.0%, respectively, confirming preferential deposition at the bottom layer followed by progressive activation of the upper layers. Therefore, the SWA architecture effectively suppresses internal short-circuiting, even during high-capacity Zn deposition.

To examine the Zn plating/stripping cycling stability, Zn||CF half-cell tests were performed at a moderate Zn capacity (30.25 mAh cm^{-2}) to avoid the earlier deterioration of the Zn counterpart. Figure 3a reveals that the cell with bare CF exhibited significant Zn CE fluctuations, showing an average Zn CE of 95.1% over 100 cycles. In contrast, the SWA cell demonstrated high stability, maintaining an average CE of 99.2%, which is attributed to bottom-to-top Zn deposition. After 100 cycles, optical images of the bare CF and SWA electrodes were acquired from the cells (Figures S6 and S7). The bare CF electrode showed accelerated dendrite formation in the top region, whereas Zn plating and stripping in the SWA electrode occurred uniformly within the bottom layer, leaving the middle and top CF layers electrochemically inactive. The superior electrochemical stability of the SWA electrode was further supported by the stable voltage profiles observed between the 10th and 100th cycles, in contrast to the significant voltage fluctuations seen in the bare CF (Figure 3b,c). Therefore, the SWA electrode enables stable Zn plating/stripping without CE loss, motivating further cycling validation in an FL-ZBB full-cell configuration.

A stress cycling test was carried out in an FL-ZBB full-cell configuration at 20 mA cm^{-2} for further comparison. To minimize the influence of Br_2 crossover and isolate the degradation caused by Zn dendrite formation, the full-cell tests were conducted using a 2.8 M $ZnBr_2$ electrolyte containing 0.5 M 1-methyl-1-ethylpyrrolidinium bromide (MEPBr) as the bromine capturing

16136829, 2026, 15, Downloaded from https://onlinelibrary.wiley.com/doi/10.1002/smll.202510641 by Daegu Gyeongbuk Institute Of, Wiley Online Library on [22/07/2026]. See the Terms and Conditions (https://onlinelibrary.wiley.com/terms-and-conditions) on Wiley Online Library for rules of use; OA articles are governed by the applicable Creative Commons License

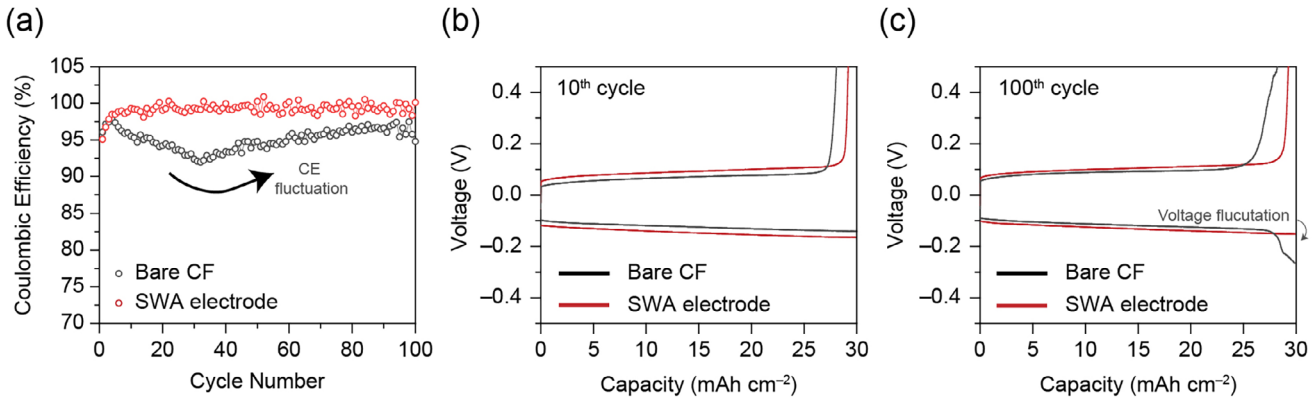

FIGURE 3 | (a) Zn reversibility and stability assessment under 5 mA cm^{-2}, 30.25 mAh cm^{-2} conditions. (b,c) Voltage profile comparisons of bare CF and SWA electrode at the 10^{th} and 100^{th} cycles in the Zn||CF half-cell test with 5, 30.25 mAh cm^{-2} condition.

agent (BCA) [37]. BCA additives such as MEPBr are widely employed in FL-ZBBs to stabilize Br_2 and suppress Br species crossover-induced self-discharge and side reactions. Owing to the absence of Br-containing species in the half-cell cycling, BCA incorporation is required only in the full-cell system, where suppressing Br-related parasitic reactions is essential for accurately evaluating Zn deposition/stripping reversibility. Despite the minimized Zn utilization (0.67%), the FL-ZBB with bare CF delivered a lower average CE of 96.3% over 10 000 cycles, whereas the SWA-based cell exhibited enhanced performance with a CE of 97.5%. Energy efficiency (EE), which reflects the overall reversibility of the cell by combining CE and voltage efficiency (VE), was comparable for both cells (~68%) at the beginning (Figure 4a). However, the bare CF cell showed a sharp EE decline within 1000 cycles, eventually dropping to 49%. In contrast, the cell with the SWA electrode exhibited robust cycling performance, with no noticeable decrease even after 10 000 cycles. Owing to the negligible change in CE, the EE decay of the bare CF cell is attributed to a reduction in VE. Br_2 generated at the positive electrode during charging typically diffuses to the negative electrode due to the inter-electrode chemical potential difference, causing self-reduction with Zn metal and resulting in CE loss [7]. Accordingly, the overpotential increase in bare CF is mainly ascribed to 'dead' Zn buildup and cumulative Br_2 side-reaction products. Indeed, the charge–discharge overpotential of the bare CF cell increases markedly from 450 to 880 mV within 1,000 cycles (Figure 4b), whereas the SWA cell shows only a minimal increase (Figure 4c). This, in turn, suggests that SWA-guided Zn deposition suppresses 'dead' Zn formation, thereby mitigating Br_2 crossover-driven Zn corrosion.

To further assess the practical viability of the SWA electrode architecture, full-cell FL-ZBBs were cycled at a high Zn utilization (33%), corresponding to an ultra-high areal capacity (100 mAh cm^{-2}), achieved for the first time [7]. While such conditions offer significant gains in energy density, they also pose considerable challenges to electrochemical stability. High Zn utilization increases the total amount of Zn deposited, which can impair the uniformity of plating/stripping behavior and promote Zn dendrite growth. Indeed, the bare CF cell failed at an early stage due to dendrite-induced internal short-circuiting, as evidenced by severe voltage fluctuations (Figure 5a), whereas the SWA cell demonstrated stable cycling, maintaining smooth and consistent charge–discharge voltage profiles over 20 cycles (Figure 5b). This highlights the necessity of the SWA-guided bottom-up Zn deposition for practical feasibility. Moreover, the bare CF cell exhibited a markedly lower discharge capacity compared to the SWA cell, likely due to bromine crossover. Excessive growth of Zn dendrites can reduce interelectrode spacing, thereby increasing the risk of bromine crossover. These unfavorable conditions hinder efficient redox cycling and ultimately compromise the long-term stability. As shown in Figure 5d,e, the cell with bare CF experienced a sharp decline in CE (from 73.0% to 40.2%) and EE (from 63.0% to 36.2%) within the first five cycles. In contrast, the SWA cell consistently maintained its initial CE and EE (72.5% and 61.9%, respectively) throughout cycling, achieving average values of 78.4% and 67.0%, respectively. Reflecting these efficiency differences, the volumetric energy densities calculated at the 10th cycle were 32.1 Wh L^{-1} for the bare CF cell and 60.4 Wh L^{-1} for the SWA cell. This significant disparity confirms that the SWA architecture enables stable operation with sustained high energy density particularly under ultra-high capacity conditions. This robust performance under demanding high-capacity conditions highlights the structural stability of the SWA electrode and underscores its potential for practical application in high-energy FL-ZBB systems.

3 | Conclusion

In this work, we propose an SWA-guided bottom-up Zn deposition strategy to enable stable cycling under high-capacity conditions. The notorious top-plating issue commonly observed in 3D Zn hosts is effectively suppressed by periodically inserting insulating porous membranes between stacked CF layers. These membranes guide preferential Zn deposition directly beneath the CF layer, where electrical connectivity is secured. The membrane is intentionally designed to permit partial Zn penetration during the deposition process, thereby electrically bridging the separated CF layers. This enables bottom-to-top sequential Zn deposition and maximizes the volumetric utilization of 3D Zn host. Indeed, SWA-guided bottom-up Zn deposition markedly suppresses excessive "dead" Zn, improving Zn CE to 99.2% (vs. 94.8% for bare CF). It also enables reliable cycling without noticeable decay in CE or EE over 10 000 cycles in FL-ZBB cells. Notably, we demonstrate for the first time the operability of a

16136829, 2026, 15, Downloaded from https://onlinelibrary.wiley.com/doi/10.1002/smll.202510641 by Daegu Gyeongbuk Institute Of, Wiley Online Library on [22/07/2026]. See the Terms and Conditions (https://onlinelibrary.wiley.com/terms-and-conditions) on Wiley Online Library for rules of use; OA articles are governed by the applicable Creative Commons License

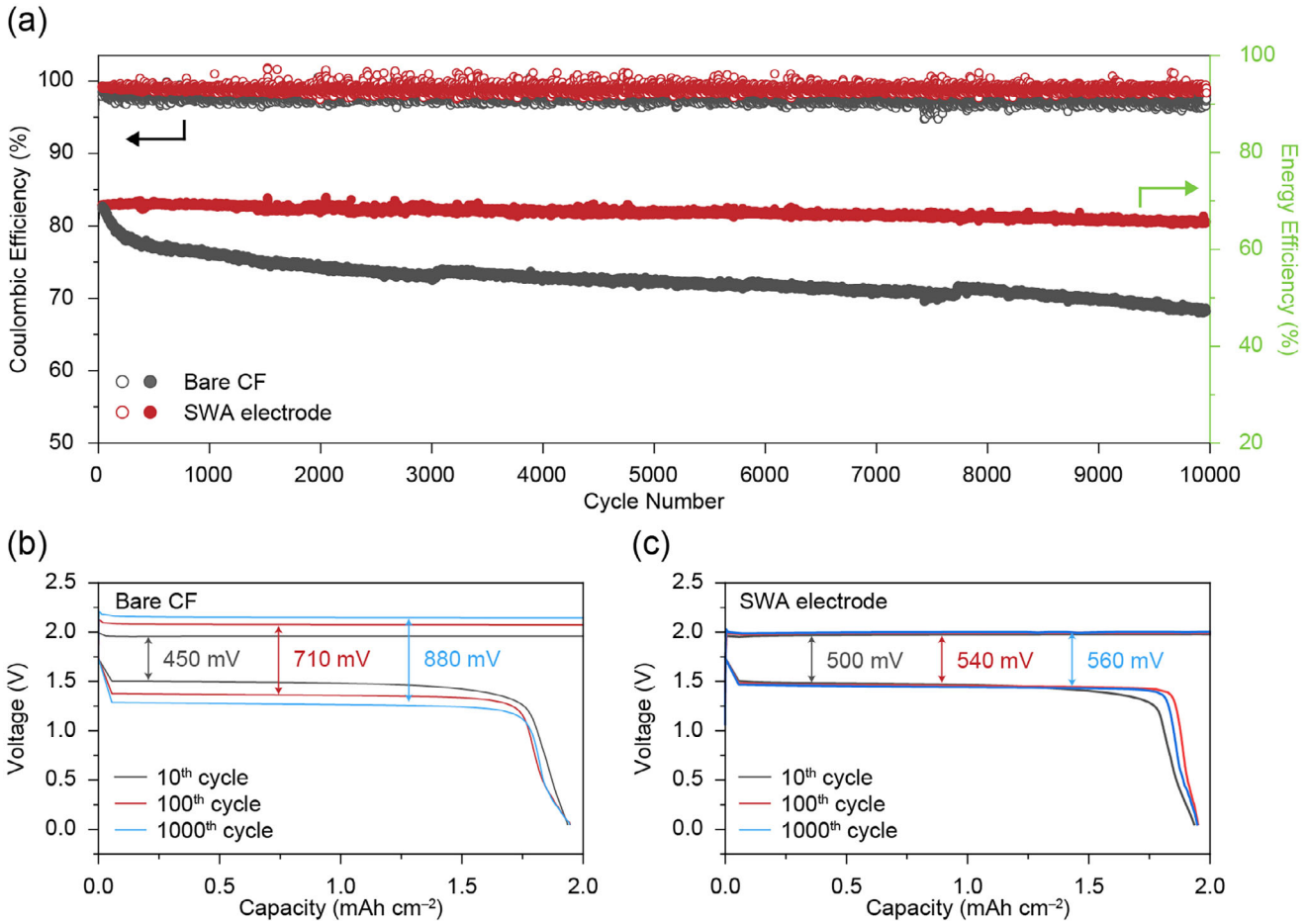

FIGURE 4 | (a) Galvanostatic cycling of FL-ZBBs employing bare CF and SWA electrodes under stress cycling condition (20 mA cm^{-2}, 2 mAh cm^{-2}) for evaluating CE and EE over long-term cycling. The charge-discharge voltage profiles of FL-ZBBs with (b) bare CF and (c) SWA electrodes at 10^{th}, 100^{th}, and 1000^{th} cycles.

simple SWA electrode under conditions previously unattainable with conventional CF, achieving 33% active materialutilization and an ultra-high areal capacity of 100 mAh cm^{-2}. Apart from the current SWA design is proof-of-concept, inter-membrane should be further optimized for controlled Zn penetration, reliable inter-layer bridging, and regulated Zn stripping to enhance reversibility and cycle life. Together with its configurational merits over traditional flow batteries, we anticipate that this simple, scalable SWA framework will open new possibilities for FL-ZBBs and be extendable to diverse redox chemistries.

4 | Methods

4.1 | Cell platform Design for Electrochemical Test

To evaluate the FL-ZBB, a custom-designed single cell structure was utilized. Each single cell was composed of two bipolar plates, Cu current collectors, and end plates. Two pieces of CF host (4.6 mm, ceramaterial) were employed as the cathode and anode within a polytetrafluoroethylene (PTFE) chamber. The CF acted as a porous host that supported the electrochemical reactions occurring at both electrodes. At the anode side, the CF provided the conductive and porous interface required for the Zn/Zn^{2+} plating/stripping reaction. At the cathode side, the Br^-/Br_2 redox couple in the electrolyte served as the active material. Therefore, the electrochemical reactions at each electrode in the full-cell can be represented by the half-cell reactions shown below:

At the negative electrode:

$$Zn^{2+}(aq) + 2e^- \leftrightarrow Zn^0(s) \quad (E^0 = -0.76\ \text{V vs SHE}) \qquad (1)$$

At the positive electrode:

$$2Br^-(aq) + 2e^- \leftrightarrow Br_2(aq) \quad (E^0 = +1.09\ \text{V vs SHE}) \qquad (2)$$

In the half-cell evaluation, one piece of CF and a Zn foil (250 μm, Goodfellow) were used to assess the reversibility of Zn during the plating/stripping process. The CF was thermally treated in an air atmosphere at 530°C for 8 h prior to use to improve hydrophilicity and electrolyte wettability, without causing any surface changes (Figure S8) [38–40]. The electrode reaction area was uniformly controlled to 3.92 cm^2 by the PTFE chamber size. A total of 8 mL of electrolyte was evenly injected, 4 mL each at the top and bottom, through holes in the PTFE chamber. The utilization of active material was calculated based on the volume and concentration of the electrolyte. Accordingly, a 10% active material utilization corresponds to a value of 119 mAh. Similarly, active material

16136829, 2026, 15, Downloaded from https://onlinelibrary.wiley.com/doi/10.1002/smll.202510641 by Daegu Gyeongbuk Institute Of, Wiley Online Library on [22/07/2026]. See the Terms and Conditions (https://onlinelibrary.wiley.com/terms-and-conditions) on Wiley Online Library for rules of use; OA articles are governed by the applicable Creative Commons License

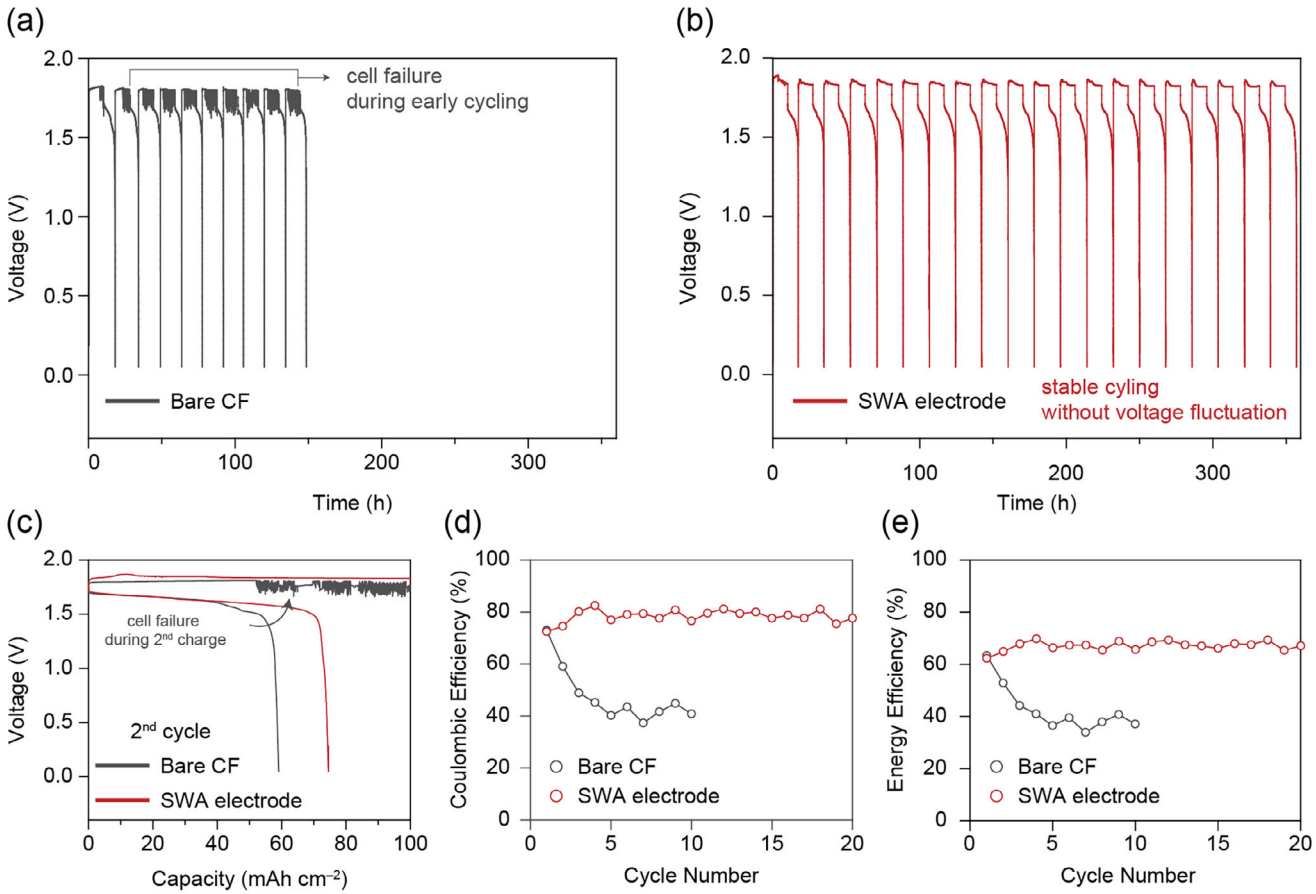

FIGURE 5 | Voltage profiles of (a) bare CF and (b) SWA electrode during high-active material utilization conditions of FL-ZBB full-cell test at 10 mA cm^{-2}, 100 mAh cm^{-2} (utilization 33%). (c) Voltage profile of second cycle, (d) CE and (e) EE under active material utilization of 33% condition.

utilization of 33% corresponds to a value of 392 mAh, calculated using the same method.

4.2 | Characterization

To analyze the morphology of Zn electrodeposition, SEM coupled with EDX (Hitachi-SU-8020) was employed. Additionally, postmortem optical image analyses were conducted to investigate the activation and deactivation mechanisms of the SWA electrode under varying deposition capacities and current densities. To validate the SWA concept in real time, an in situ cell capable of monitoring the stripping and plating processes was fabricated. Subsequently, Zn||CP cells were assembled and observed using optical microscopy (ToupTek, SCMOS05100KPA).

4.3 | Electrochemical Test

As described earlier, all electrochemical tests were conducted using the same single-cell structure. A hydrophilic PVDF membrane (Merck Millipore, VVLP09050) and a ZrO_2 membrane were placed between the CF (or Zn foil) to prevent internal short circuits. Specifically, the ZrO_2 membrane was incorporated to mechanically suppress Zn dendrite growth [41]. For short-circuit time (T_{sc}) test, NKK cellulose membrane beyond battery), GF/F (Whatman), and PP3501 (Celgard) were utilized. Electrolyte for a half cell was used with a 2.8 M $ZnBr_2$ in DI water, and in a full-cell test, 0.5 M of 1-Methyl-1-ethylpyrrolidinium bromide (MEPBr, 99%, Sigma–Aldrich) was added as a complexing agent for bromine capturing in 2.8 M $ZnBr_2$. A battery tester (WBCS3000L, WonATech) was used for electrochemical performance evaluation. All the electrochemical test were conducted in a temperature-controlled chamber maintained at 25°C

4.4 | Computational Simulation

The two dimensions of Zn deposition model was constructed using COMSOL multiphysics 6.2. The model domain was constructed by stacking VVLP layers between the three CP layers, in the sequence of bottom CP followed by VVLP, middle CP followed by VVLP, and top CP, and the thicknesses of each layer were set to 80 μm for the CP layers and 100 μm for the VVLP layers, corresponding to Figure 2a. Since the VVLP acts as an insulating layer, a columnar structure representing Zn dendrites was incorporated to provide a conductive pathway between the bottom CP and the middle CP. Both the CP and VVLP layers were porous media, allowing Zn^{2+} ion to migrate through the structure. Based on material's property, the CP layers were assigned a high electrical conductivity, whereas the VVLP layers were insulated to prevent any electronic conduction between adjacent CP layers. Zn electrodeposition reaction in the model was expressed following equation: $Zn^{2+} + 2e^- \rightarrow Zn$ which reflected the acidic electrolyte

16136829, 2026, 15, Downloaded from https://onlinelibrary.wiley.com/doi/10.1002/smll.202510641 by Daegu Gyeongbuk Institute Of, Wiley Online Library on [22/07/2026]. See the Terms and Conditions (https://onlinelibrary.wiley.com/terms-and-conditions) on Wiley Online Library for rules of use; OA articles are governed by the applicable Creative Commons License

condition. The electrochemical simulation was performed under galvanostatic condition based on Nernst-Planck equation and deforming boundary method (Figure S9). Current was applied only to the bottom CP electrode, while no external current was applied to the middle or top electrodes. The electrochemical parameters used in the model are summarized in Tables S2 and S3.

Acknowledgements

This research was supported by the National Research Foundation (NRF) of Korea through Basic Science Research Program (RS-2024-00347111), and Engineering Research Center of Excellence (RS-2023-00222166) Programs funded by the Ministry of Science and ICT (MSIT). H.L. acknowledges research supports from the National Research Council of Science & Technology (NST) grant (No. 2710024139), the HRD Program for Industrial Innovation (RS-2024–00420590), Yonsei University Research Fund (2024-22-0503 and 2025-12-0055) and 2023 Joint Research Project of the Four Institutes of Science and Technology.

Conflicts of Interest

The authors declare no conflicts of interest.

Data Availability Statement

All relevant data in this article are available from the corresponding authors upon request.

References

1. S. Chu, Y. Cui, and N. Liu, "The Path towards Sustainable Energy," *Nature Materials* 16, no. 1 (2017): 16–22, https://doi.org/10.1038/nmat4834.

2. C. P. Grey and J. M. Tarascon, "Sustainability and in Situ Monitoring in Battery Development," *Nature Materials* 16, no. 1 (2017): 45–56, https://doi.org/10.1038/nmat4777.

3. D. Wang, D. Lv, H. Peng, et al., "Site-Selective Adsorption on ZnF_2/Ag Coated Zn for Advanced Aqueous Zinc–Metal Batteries at Low Temperature," *Nano Letters* 22 (2022): 1750–1758.

4. J. Elio, P. Phelan, R. Villalobos, and R. J. Milcarek, "A Review of Energy Storage Technologies for Demand-side Management in Industrial Facilities," *Journal of Cleaner Production* 307 (2021): 127322, https://doi.org/10.1016/j.jclepro.2021.127322.

5. S. Suresh, T. Kesavan, Y. Munaiah, I. Arulraj, S. Dheenadayalan, and P. Ragupathy, "Zinc–Bromine Hybrid Flow Battery: Effect of Zinc Utilization and Performance Characteristics," *RSC Advances* 4, no. 71 (2014): 37947–37953, https://doi.org/10.1039/C4RA05946H.

6. R. Kim, J. Jung, J.-H. Lee, et al., "Modulated Zn Deposition by Glass Fiber Interlayers for Enhanced Cycling Stability of Zn–Br Redox Flow Batteries," *ACS Sustainable Chemistry & Engineering* 9, no. 36 (2021): 12242–12251.

7. K. Shin, J.-H. Lee, J. Heo, and H.-T. Kim, "Current Status and Challenges for Practical Flowless Zn–Br Batteries," *Current Opinion in Electrochemistry* 32 (2022): 100898.

8. M. C. Wu, T. S. Zhao, H. R. Jiang, Y. K. Zeng, and Y. X. Ren, "High-Performance Zinc Bromine Flow Battery Via Improved Design of Electrolyte and Electrode," *Journal of Power Sources* 355 (2017): 62–68, https://doi.org/10.1016/j.jpowsour.2017.04.058.

9. J.-H. Lee, Y. Byun, G. H. Jeong, et al., "High-Energy Efficiency Membraneless Flowless Zn–Br Battery: Utilizing the Electrochemical–Chemical Growth of Polybromides," *Advanced Materials* 31, no. 52 (2019): 1904524.

10. A. Mahmood, Z. Zheng, and Y. Chen, "Zinc–Bromine Batteries: Challenges, Prospective Solutions, and Future," *Advanced Science* 11, no. 3 (2024): 2305561, https://doi.org/10.1002/advs.202305561.

11. S. Hee Han, S. Kim, H. Yong Lim, et al., "Modified Viologen-assisted Reversible Bromine Capture and Release in Flowless Zinc–bromine Batteries," *Chemical Engineering Journal* 464 (2023): 142624.

12. S. Biswas, A. Senju, R. Mohr, et al., "Minimal Architecture Zinc–bromine Battery for Low Cost Electrochemical Energy Storage," *Energy & Environmental Science* 10, no. 1 (2017): 114–120.

13. B. Evanko, S. J. Yoo, J. Lipton, et al., "Stackable Bipolar Pouch Cells With Corrosion-resistant Current Collectors Enable High-power Aqueous Electrochemical Energy Storage," *Energy & Environmental Science* 11, no. 10 (2018): 2865–2875, https://doi.org/10.1039/C8EE00546J.

14. Y. Yin, Z. Yuan, and X. Li, "Rechargeable Aqueous Zinc–bromine Batteries: An Overview and Future Perspectives," *Physical Chemistry Chemical Physics* 23, no. 46 (2021): 26070–26084.

15. N. S. Alghamdi, M. Rana, X. Peng, et al., "Zinc–Bromine Rechargeable Batteries: From Device Configuration, Electrochemistry, Material to Performance Evaluation," *Nano-Micro Letters* 15, no. 1 (2023): 209, https://doi.org/10.1007/s40820-023-01174-7.

16. E. Ballas, A. Nimkar, G. Bergman, et al., "Self-Discharge in Flowless Zn-Br_2 Batteries and Its Mitigation," *Energy Storage Materials* 70 (2024): 103461, https://doi.org/10.1016/j.ensm.2024.103461.

17. D. Han and S. Shanmugam, "Recent Advances in the Hybrid Cathode for Rechargeable Zinc-bromine Redox Batteries," *Current Opinion in Electrochemistry* 45 (2024): 101485, https://doi.org/10.1016/j.coelec.2024.101485.

18. M. Rana, N. Alghamdi, X. Peng, et al., "Scientific Issues of Zinc-Bromine Flow Batteries and Mitigation Strategies," *Exploration* 3, no. 6 (2023): 20220073, https://doi.org/10.1002/EXP.20220073.

19. M. Lee, H. Lee, J. Han, C. Kim, and H. Lee, "Current-mediated Suppression of Hydrogen Evolution Reaction in Determination of Zn-metal Coulombic Efficiency," *Current Opinion in Electrochemistry* 47 (2024): 101571, https://doi.org/10.1016/j.coelec.2024.101571.

20. B. G. Kim, S. W. Park, H. J. Choi, J.-W. Park, H. Lee, and J.-H. Choi, "Highly Reversible Cycling of Zn-MnO_2 Batteries Integrated With Acid-Treated Carbon Supportive Layer," *Small Methods* 6, no. 2 (2022): 2101060, https://doi.org/10.1002/smtd.202101060.

21. H. Lee, J. Kang, H. W. Kang, et al., "A Hydrophilic Janus-faced Separator With Functionalized Nanocarbon for Stable Cycling of Aqueous Zn-metal Batteries," *Journal of Materials Chemistry A* 12, no. 6 (2024): 3623–3632, https://doi.org/10.1039/D3TA06268F.

22. J. Han, J. Lee, H. Lee, et al., "In-Situ Coating of Metal Fluoride/Polymer bi-Layer Protection for Dendrite-Free, Anti-Corrosive Zn-Metal Anode," *Chemical Engineering Journal* 485 (2024): 149881, https://doi.org/10.1016/j.cej.2024.149881.

23. Q. Yang, Q. Li, Z. Liu, et al., "Dendrites in Zn-Based Batteries," *Advanced Materials* 32, no. 48 (2020): 2001854, https://doi.org/10.1002/adma.202001854.

24. S. Liu, J. Wu, J. Huang, X. Chi, J. Yang, and Y. Liu, "A High-energy Efficiency Static Membrane-free Zinc–bromine Battery Enabled by a High Concentration Hybrid Electrolyte," *Sustainable Energy & Fuels* 6, no. 4 (2022): 1148–1155.

25. Y. Zhang, G. Wang, F. Yu, et al., "Highly Reversible and Dendrite-free Zn Electrodeposition Enabled by a Thin Metallic Interfacial Layer in Aqueous Batteries," *Chemical Engineering Journal* 416 (2021): 128062, https://doi.org/10.1016/j.cej.2020.128062.

26. H. R. Jiang, M. C. Wu, Y. X. Ren, W. Shyy, and T. S. Zhao, "Towards a Uniform Distribution of Zinc in the Negative Electrode for Zinc Bromine Flow Batteries," *Applied Energy* 213 (2018): 366–374, https://doi.org/10.1016/j.apenergy.2018.01.061.

27. Y. Yin, S. Wang, Q. Zhang, et al., "Dendrite-Free Zinc Deposition Induced by Tin-Modified Multifunctional 3D Host for Stable Zinc-Based

16136829, 2026, 15, Downloaded from https://onlinelibrary.wiley.com/doi/10.1002/smll.202510641 by Daegu Gyeongbuk Institute Of, Wiley Online Library on [22/07/2026]. See the Terms and Conditions (https://onlinelibrary.wiley.com/terms-and-conditions) on Wiley Online Library for rules of use; OA articles are governed by the applicable Creative Commons License

Flow Battery," *Advanced Materials* 32, no. 6 (2020): 1906803, https://doi.org/10.1002/adma.201906803.

28. J.-H. Lee, R. Kim, S. Kim, et al., "Dendrite-free Zn Electrodeposition Triggered by Interatomic Orbital Hybridization of Zn and Single Vacancy Carbon Defects for Aqueous Zn-based Flow Batteries," *Energy & Environmental Science* 13, no. 9 (2020): 2839–2848, https://doi.org/10.1039/D0EE00723D.

29. Z. Shen, L. Luo, C. Li, et al., "Stratified Zinc-Binding Strategy Toward Prolonged Cycling and Flexibility of Aqueous Fibrous Zinc Metal Batteries," *Advanced Energy Materials* 11, no. 16 (2021): 2100214, https://doi.org/10.1002/aenm.202100214.

30. J. Yun, B.-K. Park, E.-S. Won, et al., "Bottom-Up Lithium Growth Triggered by Interfacial Activity Gradient on Porous Framework for Lithium-Metal Anode," *ACS Energy Letters* 5, no. 10 (2020): 3108–3114, https://doi.org/10.1021/acsenergylett.0c01619.

31. M. Zhang, Y. Deng, Y. Yan, H. Mei, L. Cheng, and L. Zhang, "Spatially Restricted Deposition of Zn Metal in Localized-Activation 3D Electrode Enables Long-Term Stable Zinc Ion Batteries," *Energy Storage Materials* 65 (2024): 103156, https://doi.org/10.1016/j.ensm.2023.103156.

32. P. X. Sun, Z. Cao, Y. X. Zeng, et al., "Formation of Super-Assembled TiOx/Zn/N-Doped Carbon Inverse Opal Towards Dendrite-Free Zn Anodes," *Angewandte Chemie International Edition* 61 (2022): 202115649.

33. B. Zakeri and S. Syri, "Electrical Energy Storage Systems: A Comparative Life Cycle Cost Analysis," *Renewable and Sustainable Energy Reviews* 42 (2015): 569–596, https://doi.org/10.1016/j.rser.2014.10.011.

34. G. P. Rajarathnam, M. E. Easton, M. Schneider, A. F. Masters, T. Maschmeyer, and A. M. Vassallo, "The Influence of Ionic Liquid Additives on Zinc Half-Cell Electrochemical Performance in Zinc/Bromine Flow Batteries," *RSC Advances* 6, no. 33 (2016): 27788–27797, https://doi.org/10.1039/C6RA03566C.

35. X. Wu, S. Liu, N. Wang, S. Peng, and Z. He, "Influence of Organic Additives on Electrochemical Properties of the Positive Electrolyte for All-Vanadium Redox Flow Battery," *Electrochimica Acta* 78 (2012): 475–482, https://doi.org/10.1016/j.electacta.2012.06.065.

36. H. An, Y. Roh, Y. Jo, et al., "Separator Dependency on Cycling Stability of Lithium Metal Batteries under Practical Conditions," *Energy & Environmental Materials* 6, no. 5 (2023): 12397, https://doi.org/10.1002/eem2.12397.

37. H.-T. Kim, J.-H. Lee, D. S. Kim, and J. H. Yang, *Redox Flow—Zn–Br. in Encyclopedia of Electrochemistry*, ed. A.J. Bard, (Wiley, 2020), 1–38.

38. Y.-H. Lee, K. Shin, J. Baek, and H.-T. Kim, "Boosting the Kinetics of Bromine Cathode in Zn–Br Flow Battery by Enhancing the Electrode Adsorption of the Droplet of Bromine Sequestration Agent/Polybromides Complex," *Journal of Power Sources* 620 (2024): 235219.

39. K. Mariyappan, R. Velmurugan, B. Subramanian, P. Ragupathy, and M. Ulaganathan, "Low Loading of Pt@Graphite Felt for Enhancing Multifunctional Activity towards Achieving High Energy Efficiency of Zn–Br_2 Redox Flow Battery," *Journal of Power Sources* 482 (2021): 228912.

40. Z. Xu, J. Li, and M. Wu, "A High-Rate and Long-Life Zinc-Bromine Flow Battery," *Journal of Power Sources* 613 (2024): 234869, https://doi.org/10.1016/j.jpowsour.2024.234869.

41. J. Kim, H. Park, Y. Cho, et al., "Stable Zinc Electrode Reaction Enabled by Combined Cationic and Anionic Electrolyte Additives for Non-Flow Aqueous Zn—Br_2 Batteries," *Small* 20 (2024): 2401916.

Supporting Information

Additional supporting information can be found online in the Supporting Information section.

Supporting File: smll72418-sup-0001-SuppMat.docx.

16136829, 2026, 15, Downloaded from https://onlinelibrary.wiley.com/doi/10.1002/smll.202510641 by Daegu Gyeongbuk Institute Of, Wiley Online Library on [22/07/2026]. See the Terms and Conditions (https://onlinelibrary.wiley.com/terms-and-conditions) on Wiley Online Library for rules of use; OA articles are governed by the applicable Creative Commons License